SCIENTIFIC REPORTS

OPEN

SUBJECT AREAS:
PHOTOCATALYSIS
CATALYST SYNTHESIS

Received
30 May 2014

Accepted
25 July 2014

Published
9 September 2014

Correspondence and requests for materials should be addressed to G.K.Z. (gkzhang@whut.edu.cn)

Controlled synthesis and visible light photocatalytic activity of $Bi_{12}GeO_{20}$ uniform microcrystals

Zhen Wan & Gaoke Zhang

School of Resources and Environmental Engineering, Wuhan University of Technology, Wuhan, 430070, China.

We successfully synthesized uniform $Bi_{12}GeO_{20}$ microspheres and microtetrahedrons enclosed by four {111} facets using a controlled hydrothermal method for the first time. The photocatalytic activity of these regular-shaped products was further investigated by the degradation of RhB and gaseous formaldehyde under visible light irradiation (λ>420 nm). The $Bi_{12}GeO_{20}$ microtetrahedrons (s) exhibited enhanced photocatalytic activity and stability which is closely related to the high capacity of exposed {111} facets for uptake of O_2. The formation mechanism studies indicate that the $Bi_{12}GeO_{20}$ seeds were directed to grow into truncated microcubes, truncated microtetrahedrons, and then microtetrahedrons when the NaOH concentration was 5 M. The same batch of seeds only evolved into microspheres when the NaOH concentration was switched to 3 M. The difference in $Bi_{12}GeO_{20}$ morphology could be attributed to the rates of both crystal nucleation and crystal growth.

It is known that the control over shape as well as exposed facets of nanoscale and micrometer scale semiconductor materials represents a great challenge in realizing the design of novel functional devices[1–3]. This is due to the shape as well as exposed facets of these materials have significant effects on their properties, which ultimately determine the practical applications[4–7]. In this regard, remarkable progress has been made for the controlled synthesis and self-organization of inorganic materials with regular geometrical shapes and active exposed facets, whether in the dimensions of nano or micrometer scale[8–12]. These materials may provide opportunities to exploit novel properties because of their large surface area and high surface permeability[13–14]. Particularly, extensive research has been done in the synthesis of photocatalysts with tunable shape and specific exposed facets.

The synthesis and application of photocatalysts have been studied to tackle the global energy demand and environmental pollution problems[15]. Among them, high-efficient and non-toxic photocatalysts of metal oxides for converting solar energy into chemical energy have been paid much more attentions recently[16–17]. Based on the electronic configuration of their core metal ions, these photocatalysts are divided into three groups: transition metal ions with d^0 configuration, rare-earth metal ions with f^0 configuration, and typical metal ions with d^{10} configuration[18]. Since the transition-metal ion of Bi^{3+} possesses the same electronic configuration as Ga^{3+} and Sn^{4+} in several typical photocatalysts, Bi-based oxides are suggested to be the viable photocatalysts and have been widely investigated[19–20]. In this area, bismuth germanate ($Bi_{12}GeO_{20}$), which belongs to the sillenite group of cubic crystals of the I23 space group, has attracted considerable interests nowadays[21]. For the crystal structure of $Bi_{12}GeO_{20}$ (BGO), The Ge atoms occupy geometrically regular tetrahedral sites, and the Bi atoms are hepta-coordinated, which means that five oxygen atoms form an incomplete octahedral arrangement, and the remaining two oxygen atoms are electrostatically coordinated, on either side of the 6 s^2 lone electron pair in Bi^{3+} [22]. The BGO exhibits strong photoconductivity under illumination for its considerable mobility of the photo-generated carriers[23], which fits the essential demand for an effective photocatalyst. However, the successive modulation of shape as well as exposed facets of BGO products has yet to become reality. For photocatalysts, the high-energy conversion efficiencies as well as large light harvesting capacities can be achieved by the control over the shape and exposed facets[24]. Thus, the controlled synthesis of BGO products with novel morphology and exposed special facets still remains a great challenge.

In this paper, uniform $Bi_{12}GeO_{20}$ microspheres and microtetrahedrons enclosed by four {111} facets (shown in Table 1) were synthesized via a one-step hydrothermal process. For comparison, pure $Bi_{12}GeO_{20}$ nanoparticles were prepared by a sol-gel reaction (Supplementary Information). These samples were noted as BGO microspheres, BGO microtetrahedrons, BGO microtetrahedrons (s) and BGO-NP. The influences of reaction condi-

Table 1 | The synthesis conditions and optical-bandgaps of as-prepared BGO microcrystals

BGO microcrystals	NaOH concentration	Additive	Band gap	Morphology
BGO microspheres	3 M	None	2.71 eV	Microsphere
BGO microtetrahedrons	5 M	None	2.30 eV	Microtetrahedron
BGO microtetrahedrons (s)	5 M	CTAB	2.65 eV	Microtetrahedron

tions on the shape and exposed facets of as-prepared products have been systematically investigated and the photocatalytic property has been studied in detail. The formation mechanism and shape-evolution process of the as-prepared products have been also discussed in detail.

Results

Structure and morphology. The phase composition and crystal structure of the products prepared under different conditions were examined by powder X-ray diffraction (XRD). As shown in Figure 1a, the diffraction peaks of these samples agree well with those of the pure $Bi_{12}GeO_{20}$ according to the JCPDS card no.77-0861. The strong and sharp diffraction peaks imply good crystallinity of the products and no other impurity peaks were detected. The XRD pattern of the BGO-NP (Supplementary Information, Figure S1) is also in accord with the JCPDS card no.77-0861. The results indicate that well-crystallized single phase $Bi_{12}GeO_{20}$ had been successfully synthesized under the current experimental conditions. According to the XRD patterns, the $Bi_{12}GeO_{20}$ structure is cubic and it was modeled as Figure 1b, with a lattice constant of 10.013 Å and a total of 66 atoms in a supercell[18].

The surface composition and chemical state of the as-prepared BGO samples were further investigated using X-ray photoelectron spectroscopy (XPS). As shown in the XPS survey spectrum (Figure 1c), the O 1s, Bi $4f_{7/2}$, Bi $4f_{5/2}$, Ge 3d and Bi 5d binding energy peaks were detected. In Figure 1d, the O 1s binding energy peak at around 529.4 eV is attributed to bridging oxygen atoms from Bi-O-Bi bonds[25]. From the Bi 4f region in Figure 1e, the peaks at 158.4 and 163.7 eV are attributed to the binding energies of the Bi $4f_{7/2}$ and Bi $4f_{5/2}$ levels respectively, which correspond to Bi^{3+} according to the previous reports[26]. In Figure 1f, the peak at 25.4 eV is assigned to Bi 5d and the peak at 28.7 eV is assigned to Ge 3d, indicating germanium in the sample exists in the form of Ge^{4+} [27]. The XPS analysis results further demonstrate the composition of BGO microcrystals.

The morphology and size of BGO microcrystals were investigated by scanning electron microscopy (SEM), transmission electron microscopy (TEM) and high-resolution transmission electron microscopy (HRTEM). The morphological and dimensional changes of the as-prepared BGO samples were observed for the first time, which strongly depended on the NaOH concentration. In Figure 2a, it can be seen that the BGO products after 12 h hydrothermal reaction show a spherical microstructure with an average diameter of 8 μm when the NaOH concentration was 3 M. The inset higher magnification image indicates that the microspheres consist of large amounts of small particles. In Figure 2b, it can be seen that the BGO products obtained at 5 M NaOH after 12 h hydrothermal reaction exhibit regular tetrahedron-shape morphology with an average edge length of 20 μm. The four outer facets of the as-synthesized tetrahedron-shape structure could be indexed to the {111} crystal facets[28]. Interestingly, it can be seen from Figure 2c that smooth and well-defined BGO microtetrahedrons (s) could be obtained with average edge length of about 8 μm when CTAB existed in the hydrothermal process with 5 M NaOH. Meanwhile, BGO nanoparticles with an average diameter of 80 nm were shown in Figure S2 (Supplementary Information). The microstructures of the BGO microtetrahedrons (s) were further examined by TEM and HRTEM. Figure 2d is a corresponding high-resolution TEM (HRTEM) image near the edge of the BGO microtetrahedrons (s). The regular lattice spacing of 0.36 nm is consistent with the (220) crystal plane of BGO crystal (JCPDS no. 77-0861). The result shows the BGO microtetrahedrons (s) can be synthesized by a simple route in the presence of CTAB.

UV-vis diffuse reflectance spectra analysis. It is well-known that the optical absorption performances of semiconductors are relevant to the electronic structure feature and are the key factors in determining their photocatalytic activities. The UV-visible diffuse reflectance spectra in the wavelength range of 200–800 nm for the BGO products are shown in Figure 3a. The band gap energy (E_g) of the semiconductor can be estimated by the formula: $E_g = 1240/\lambda_g$, where λ_g is the wavelength corresponding to the intersection point of the vertical and horizontal parts of the spectrum. In the Figure 3a, the absorption spectra show that all BGO products can absorb considerable amounts of visible light, suggesting their potential applications as visible light driven photocatalysts. Besides, the Figure 3a also reveals that the absorption spectra in the visible region are not very steep and all has a tail in the edge, which reveals that the visible light absorption should be not due to an intrinsic band-to-band transition but due to an impurity or defect level transition[21]. From the Figure 3a, the band gaps are determined to be 2.71 eV for BGO microspheres, 2.30 eV for microtetrahedrons, and 2.65 eV for microtetrahedrons (s) respectively (as shown in Table 1), which are quite comparable with previous results[29–30]. For the BGO products (microspheres, microtetrahedrons (s) and microtetrahedrons), the color turned yellow successively, which is corresponding to the changes of their band gaps. The obvious shift for the band gaps of the products might be attributed to the change of size and the different morphology[31–33].

It has been reported that $Bi_{12}GeO_{20}$ crystal is a wide-band gap material with an E_g of about 3.2 eV at 300 K, which can only be driven by UV light[34]. In the Figure 3a, the strong absorption in the visible light region from the absorption spectra indicates the existence of defect energy level in the forbidden gap[21]. The electrons (holes) could transfer between the defect energy level and the conduction band (CB)/valence band (VB) under visible light irradiation. Finally, holes in the VB or electrons in the CB were generated, followed either by recombination to release heat, or migration into the surface to react with a suitable electron acceptor and donor.

Photocatalytic activity. RhB aqueous solution and gaseous formaldehyde were chosen as the model organic pollutant to evaluate the photocatalytic activity of the BGO products. Figure 3b displays the concentration changes of the RhB solution during the photocatalytic degradation process by various BGO products under visible light irradiation. The photolysis of the RhB solution was negligible in the absence of photocatalyst, indicating that the exposure of the RhB solution to visible light irradiation did not stimulate obvious self-degradation. Meanwhile, the BGO microspheres, BGO-NP and BGO microtetrahedrons exhibited weak photocatalytic activities as the concentrations of the RhB solution were only decreased by 13%, 28% and 31% respectively after visible light irradiation for 4 h. However, with the BGO microtetrahedrons (s) as the photocatalyst, the concentration of the RhB solution was decreased to 69% under the same condition, showing enhanced photocatalytic activity as compared to other three products. The photocatalytic degradation reactions could also be described by the first-order kinetics with respect to the concentration of the organic

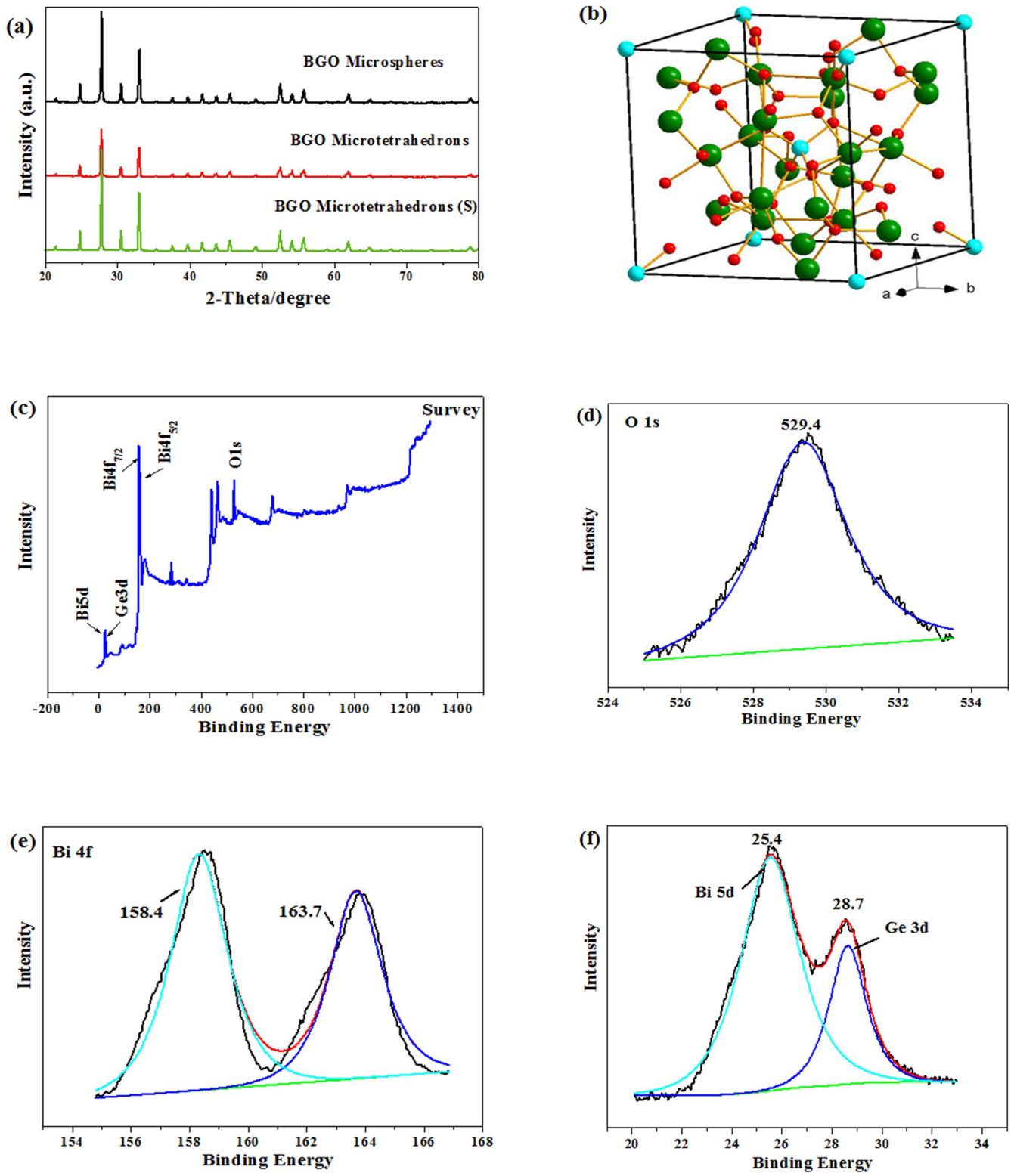

Figure 1 | (a) XRD patterns of BGO products. (b) Supercell model for BGO microcrystals. The green, blue and red spheres represent Bi, Ge and O atoms, respectively. (c) Survey XPS spectrum of BGO microtetrahedrons (s) and (d–f) high-resolution XPS spectra of O 1s, Bi 4f, Bi 5d and Ge 3d regions of BGO microtetrahedrons (s).

compound. The time-dependent decomposition of the RhB solution followed the first-order kinetics, $\ln(C_0/C) = kt$, where t is the irradiation time and k is the apparent rate constant. Figure 3c shows a comparison of the apparent rate constants for the BGO microspheres, BGO-NP, BGO microtetrahedrons and BGO microtetrahedrons (s) samples and the results are 0.034, 0.070, 0.094 and 0.290 respectively.

The photocatalytic activity of the BGO microtetrahedrons (s) for gaseous formaldehyde degradation under visible light irradiation was also tested. The results are shown in Figure 3d and 3e. From the

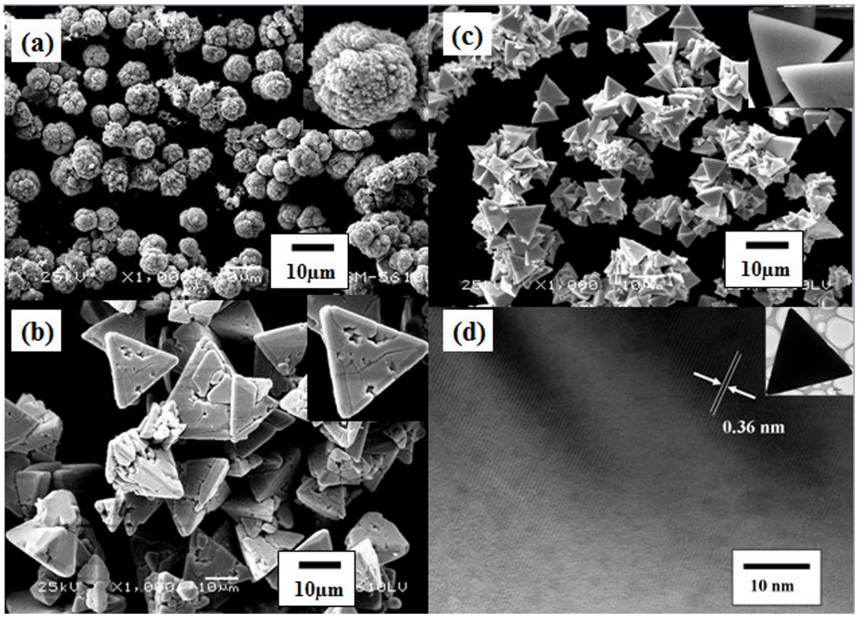

Figure 2 | SEM images of (a) BGO microspheres, (b) BGO microtetrahedrons and (c) BGO microtetrahedrons (s). (d) HRTEM image taken from an edge of a BGO microtetrahedron (s) and Inset is the TEM image of a typical BGO microtetrahedron (s).

Figure 3d, it can be seen that the gaseous formaldehyde was decomposed and the CO_2 was generated at the same time with the BGO microtetrahedrons (s) as the photocatalyst. Figure 3e displays the concentration changes of the CO_2 during the photocatalytic degradation of gaseous formaldehyde by various BGO products under visible light irradiation. The result indicates that the BGO products also exhibited relatively high photocatalytic activities for the degradation of gaseous formaldehyde.

To test the stability of the as-prepared BGO products, the recycling capability of the BGO microtetrahedrons (s) was evaluated by the degradation of the RhB solution over the reused BGO microtetrahedrons (s). As shown in Figure 3f, the catalyst did not exhibit significant loss of photocatalytic activity after four times recycling. Meanwhile, XRD and FTIR analyses show that there is no observable structural difference between the BGO microtetrahedrons (s) samples before and after photocatalytic degradation of the RhB solution (Supplementary Information, Figure S3 and S4). The above results indicate that the BGO products are effective and stable catalysts for the degradation of organic pollutants.

Discussion

On the basis of the above results, the formation of BGO microcrystals can be described by the following process. When $Bi(NO_3)_3 \cdot 5H_2O$ suspension was added into the alkaline solution (NaOH), amorphous bismuth hydroxide particles were formed, which will be located at the bottom of the autoclave. When the autoclave was heated to 180°C, solution in the autoclave was overheated and formed supercritical solution. The dissolvability of bismuth hydroxide particles in the supercritical solution was thus increased because of the novel dissoluble ability of supercritical solution[35] [equation (1)]. Meanwhile, $HGeO_3^-$ was formed in the alkaline environment [equation (2)]. When the concentrations of Bi^{3+} and $HGeO_3^-$ reached the supersaturation degree, the $Bi_{12}GeO_{20}$ small crystallites nucleated and grew into small seeds [equation (3)]. As the reaction continued, the irregular aggregates changed into tetrahedron-shape or sphere-shape microcrystals, and the larger BGO nuclei grew gradually at the cost of the smaller ones at the same time. Therefore, the formation of BGO in our experiment is believed to follow the Ostwald ripening process[36].

On the other hand, as is well-known, the size and morphology of the product depend strongly on both crystal nucleation and crystal growth[37–38]. Tetrahedron-shape microcrystals exposed with four {111} facets could only be formed under a kinetically controlled condition because of its much larger surface area to volume ratio relative to microspheres. According to the experimental results, the relatively low alkaline concentration (3 M) resulted in the poor stability of the bismuth hydroxide particles, which gave rise to the rapid release speed of Bi^{3+} ions in the solution. Nucleation occurred rapidly and large quantities of BGO microcrystals with small size were formed in the solution (Figure 2a). When the alkaline value was increased to 5 M, the high alkaline concentration resulted in the formation of stable bismuth hydroxide particles, which gave rise to the slow release speed of Bi^{3+} ions in the solution. The rapid crystal growth occurred and ultimately resulted in the formation of microtetrahedrons exposed with four {111} facets due to the lower surface free energy of {111} relative to other facets (Figure 2b). In addition, the synthesis of BGO microtetrahedrons (s) indicates that the CTAB is beneficial to reduce the tetrahedron size and smooth the surface of tetrahedron-shaped BGO. We consider that the addition of CTAB lowered the surface energy and could covalently bind to the surface atoms of the microcrystal and thus prevented them from forming bulk materials[15]. Meanwhile, the addition of CTAB reduced the corrosion of the NaOH on the exposed {111} facets of the tetrahedron-shaped BGO products during the hydrothermal process and thus smoothed the surface of the BGO microtetrahedrons (s)[32]. The shape evolution of the BGO microcrystals is illustrated in detail in Figure 4.

It has been widely observed that the photocatalytic degradation of contaminations can not proceed in the absence of O_2[39–40]. The increase of the concentration of adsorbed O_2 on the surface of catalysts would serve as an electron acceptor which facilitate the electron transfer and thus enhance the photocatalytic activity[40]. However, the amount of O_2 adsorbed on different photocatalysts might be widely divergent. A catalyst that has a high intrinsic photoactivity, but a low capacity for uptake of O_2 from water, may display a low apparent photoactivity for organic degradation. Xu et al.[41] reported that for phenol degradation in an aerated aqueous suspension, rutile TiO_2 showed lower photocatalytic activity than anatase TiO_2, but its activity became similar to or higher than that of the anatase TiO_2 on the addition of $AgNO_3$. To further investigate the difference of photocatalytic activities among BGO products, controlled experiments were carried out as shown in Figure 5. All the

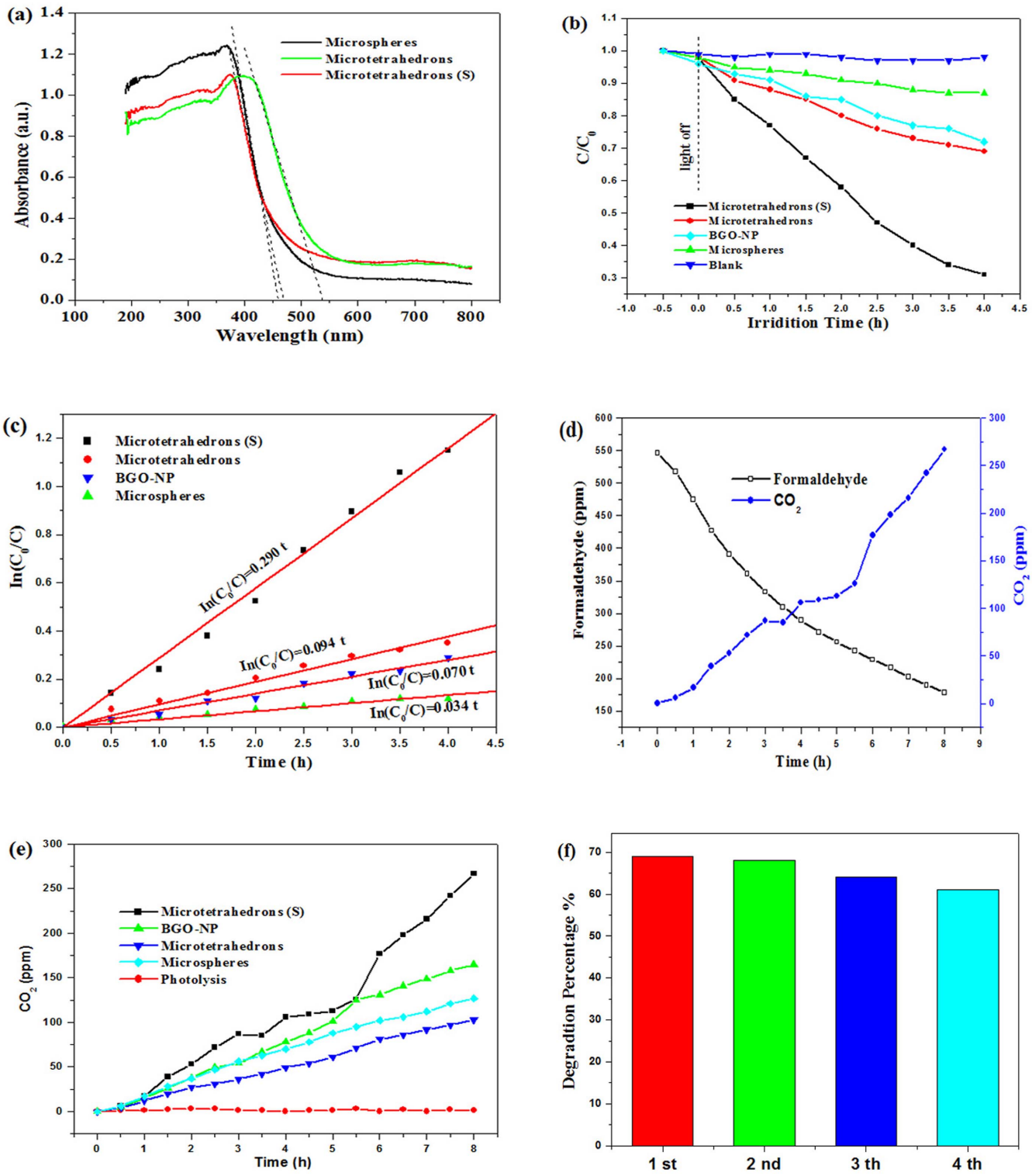

Figure 3 | (a) UV-vis diffuse reflectance spectra of BGO products. (b) Photocatalytic performances and (c) kinetic studies of the BGO products for RhB degradation under visible light irradiation. (d) Photocatalytic degradation of gaseous formaldehyde of BGO microtetrahedrons (s). (e) The concentration changes of CO_2 during the photocatalytic degradation of gaseous formaldehyde by BGO products. (f) Cycling runs of the BGO microtetrahedrons (s) for the degradation of RhB.

BGO products exhibited negative photocatalytic activities in the N_2-purged aqueous suspensions. However, when 0.1 M of $AgNO_3$ solutions were added ($Ag/Bi_{12}GeO_{20}$ =10 wt %), the BGO microspheres showed higher photocatalytic activity than other three products. In this work, Ag^+ has been used as an electron scavenger to eliminate the impact of adsorbed O_2 on the surface of catalysts to the photocatalytic reaction. Moreover, the surface atomic configurations of {111} facets in Figure 6 clearly show that only Bi and Ge atoms are contained in the {111} facets and no O atoms were observed. Based on the above results, we speculate that the enhanced photocatalytic activity of the BGO microtetrahedrons (s) is due to the high capacity of exposed {111} facets for uptake of O_2 which can be partly attrib-

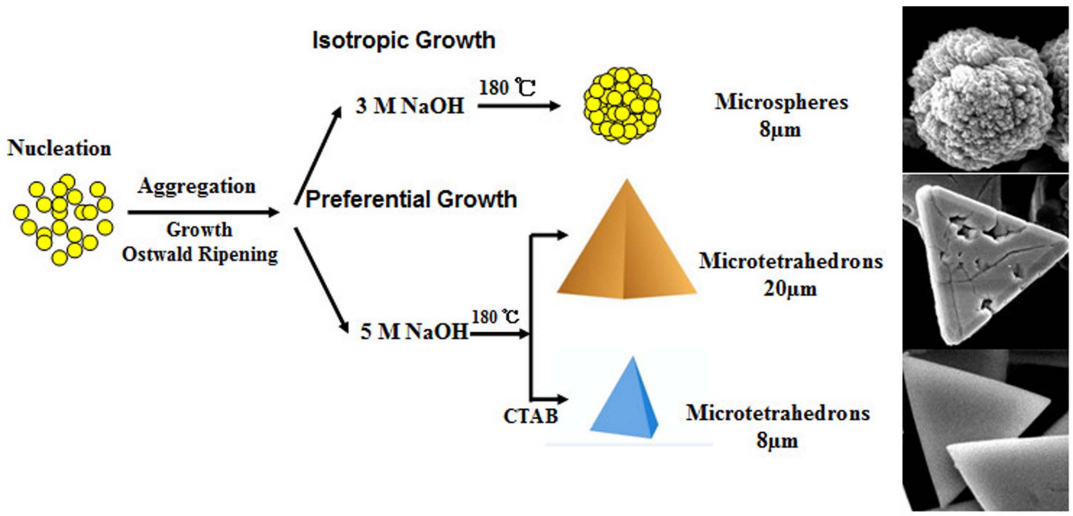

Figure 4 | **Schematic illustration of the formation and shape-evolution process of BGO microcrystals.**

uted to the lack of O atoms in the {111} facets. Compared with the BGO microtetrahedrons (s), the lower photocatalytic activity of the BGO microtetrahedrons is due to the corrosion of the NaOH on the exposed {111} facets.

In order to understand the formation mechanism of the BGO microtetrahedrons, time-dependent experiments were carried out while the other reaction conditions were kept constant. In Figure 7, the resulting products obtained at various stages of the hydrothermal process were studied by field emission scanning electron microscopy (FESEM). Figure 7a displays that both the truncated cube-shaped and truncated tetrahedron-shaped BGO microcrystals (~6 μm) were obtained after 3 h hydrothermal reaction. As the reaction continued to 6 h (Figure 7b), almost all the truncated cube-shaped and parts of the truncated tetrahedron-shaped structures disappeared. Meanwhile, the section area of truncated tetrahedron-shaped structures decreased and the tetrahedron-shaped BGO with an average diameter of about 8 μm could be clearly observed. Finally, in Figure 7c, a large amount of the perfect tetrahedron-shaped microcrystals (~20 μm) were generated with further extending the reaction time to 12 h. On the basis of the above time-dependent transformation process, the formation mechanism of the BGO microtetrahedrons was shown by the schematic illustration in Figure 8. Firstly, the truncated cube-shaped BGO microcrystals enclosed by a mix of both {111} and {100} facets on the surface were formed[42]. Secondly, the {100} facets disappeared due to the higher surface free energy of the {100} facets relative to {111} facets[43] and the truncated cube-shaped BGO microcrystals were transformed into the truncated tetrahedron-shaped structures (eight {111} facets). Thirdly, as the reaction continued, only four of the {111} facets of the truncated tetrahedron-shaped BGO microcrystals could further grow in the following step to generate perfect tetrahedron-shaped microcrystals. It is worth noting that the overgrowth only occurred on four of the eight {111} facets of the truncated tetrahedron-shaped structures as there was essentially no growth for the other four {111} facets. We considered that the newly formed BGO molecules could not be deposited on all of the eight {111} facets due to the limit of reaction rate. Once a cluster (or nucleus) of BGO molecules had been created on a certain face of a seed, the deposition of BGO molecules in the following steps would preferentially occur at this site rather than on other regions due to the lower energy barrier[43]. The site-localized growth could be retained as long as the deposition rate is faster than the surface diffusion rate[44]. Further growth of the BGO microcrystals resulted in the formation of the BGO microtetrahedrons exposed with four {111} facets.

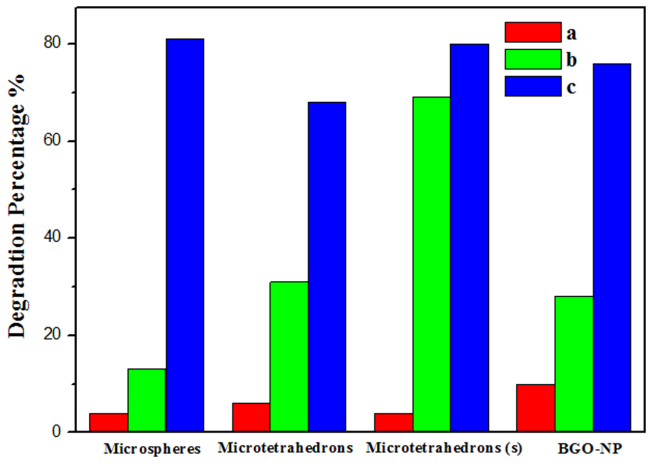

Figure 5 | **Photocatalytic degradation of RhB under different conditions: (a) in the N_2-purged aqueous suspension of as-prepared products, (b) in the aqueous suspension of as-prepared products, (c) in the N_2-purged aqueous suspension of as-prepared products and $AgNO_3$.**

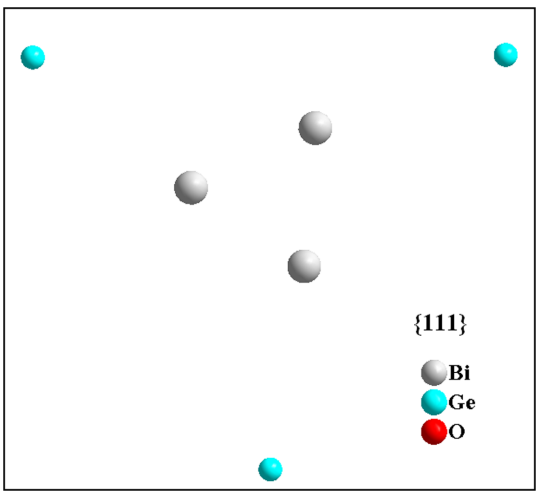

Figure 6 | **Surface atomic configurations in the {111} facets of the tetrahedron-shaped BGO products.**

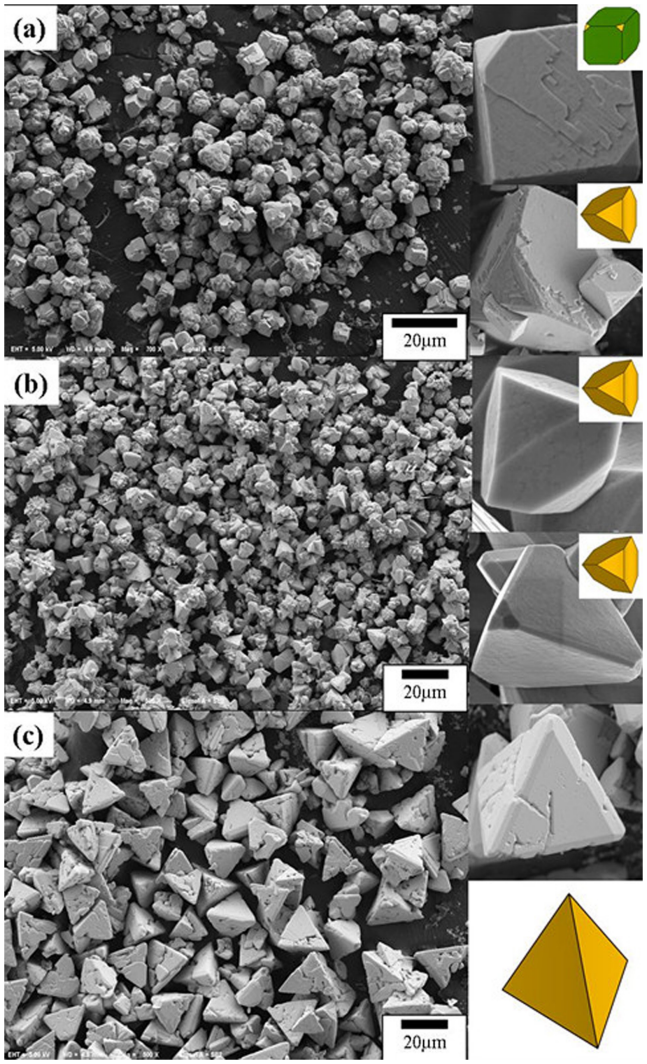

Figure 7 | FESEM images of BGO microtetrahedrons obtained with 5 M NaOH after hydrothermal treating for (a) 3 h, (b) 6 h, and (c) 12 h.

$$Bi(OH)_3 \rightarrow Bi^{3+} + 3OH^- \quad (1)$$

$$GeO_2 + OH^- \rightarrow HGeO_3^- \quad (2)$$

$$12Bi^{3+} + HGeO_3^- + 35OH^- \rightarrow Bi_{12}GeO_{20} + 18H_2O \quad (3)$$

In summary, well-defined BGO microcrystals (microspheres, microtetrahedrons and microtetrahedrons (s)) were successfully synthesized by adjusting the alkaline value or adding coordinating agent CTAB in the hydrothermal process. The microtetrahedrons (s) showed good photocatalytic activity and stability for the degradation of RhB and gaseous formaldehyde under visible light irradiation. Its enhanced photocatalytic activity is due to the high capacity of exposed {111} facets for uptake of O_2. The shape evolution of the BGO microcrystals was discussed in detail. The studies on the early stages of the BGO microtetrahedrons indicate the possible formation mechanisms of BGO microtetrahedrons. These works demonstrate that the $Bi_{12}GeO_{20}$ microcrystals are promising materials for the applications as photocatalysts and related fields in the visible range.

Methods

Synthesis of catalyst. All the reagents were of analytical purity and were used as received from Sinopharm Chemical Reagent Co., Ltd, China. In a typical synthesis, a certain amount of $Bi(NO_3)_3 \cdot 5H_2O$ (12 mmol) and GeO_2 (1 mmol) were dissolved in NaOH solution (70 mL) of different concentrations under magnetic stirring. The final concentration of NaOH was 3 or 5 M. Specially, 0.5 g of cetyltrimethyl ammonium bromide (CTAB) was added to the 5 M NaOH for the synthesis of microtetrahedrons (s). Then the mixture was transferred to a stainless steel Teflon-lined autoclave of 100 mL capacity. The autoclave was sealed and heated at 180°C for a designed period of time and then cooled to room temperature naturally. The final products were collected by centrifugation, rinsed with distilled water and ethanol, and dried at 70°C for 5 h.

Materials characterization. The structure and crystallinity of the as–prepared samples were characterized by powder X-ray diffraction (XRD) analysis on a D/MAX-RB diffractometer with Cu Ka radiation under the operation conditions of 40 kV and 50 mA. Scanning electron microscopy (SEM, JSM-5610LV) and field emission scanning electron microscopy (FESEM, S-4800) were used to characterize the morphologies of the products. The morphologies and microstructures of the prepared products were further examined by transmission electron microscopy (TEM) and high-resolution transmission electron microscopy (HRTEM) using a JEM 2100F electron microscope operated at an accelerating voltage of 200 kV. The absorption edges of the products were measured by a UV–vis spectrophotometer (UV2550, Shimadzu Corporation, Kyoto, Japan). $BaSO_4$ was used as a reflectance standard. X-ray photoelectron spectroscopy (XPS) was carried out using an ESCALAB II XPS system with a monochromatic Mg Ka source and a charge neutralizer. The binding energies obtained in the XPS spectral analysis were corrected for specimen charging by referencing C 1s to 284.5 eV. A Nexus Fourier transform infrared (FT-IR) spectroscopy (Thermo Nicolet, USA) was used to detect the chemical bonds of the samples.

Photocatalytic measurements. The photocatalytic activities of the as-prepared BGO samples were measured by the degradation of RhB aqueous solution and gaseous formaldehyde under visible light irradiation. For the degradation of RhB aqueous solution, the experiments were performed at room temperature as follows: 0.5 g of the as-prepared catalyst was added into 100 mL of RhB aqueous solution (5 mg/L). Prior to visible light illumination, the suspension was stirred for 0.5 h in dark to reach adsorption equilibrium. The reactor was then irradiated with visible light emitted by a 350 W Dy lamp with a 420 nm cutoff filter. The reaction temperature was kept at room temperature to prevent any thermal catalytic effect. At a defined time interval, the concentration of RhB aqueous solution was analyzed using a UV-vis spectrophotometer (UV751GD, China) at its maximum absorption wavelength of 553 nm.

For the degradation of gaseous formaldehyde under visible light irradiation, all experiments were carried on a closed, cylindrical, and stainless gas-phase batch reactor with a volume of 800 mL. A 350 W Dy lamp was set to irradiate the reactor, and the visible light irradiation (>420 nm) was achieved with a glass filter. The experiments were performed at room temperature as follows: 0.5 g of the as-prepared catalyst was dispersed onto the surface of a dish with a diameter of 8 cm. After the

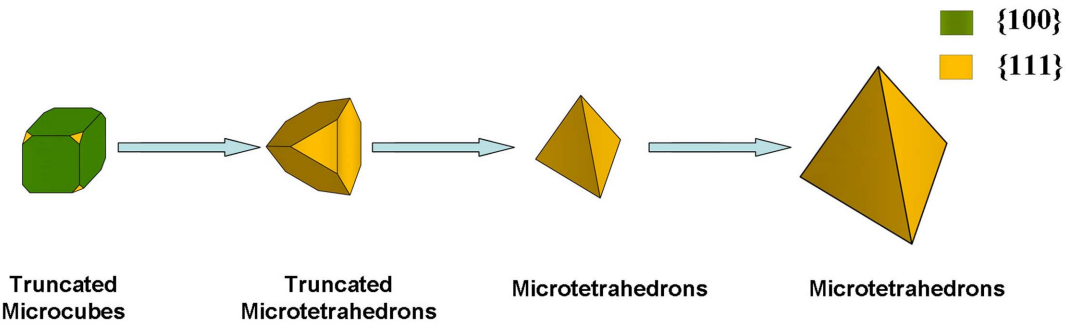

Figure 8 | Schematic illustration of the formation mechanism of BGO microtetrahedrons.

dish with catalyst was placed in the reactor, a certain amount of formaldehyde (1.5 μL) was injected with a syringe into the reactor. The lamp was not turned on until the concentration of gaseous formaldehyde remained stable. The concentrations of CO_2 and gaseous formaldehyde were measured by a 1412 photoacoustic field gas-monitor (Innova, AirTech Instruments, Denmark) per 15 min.

1. Jiao, Z. *et al*. Visible-light-driven photoelectrochemical and photocatalytic performances of Cr-doped $SrTiO_3/TiO_2$ heterostructured nanotube arrays. *Sci. Rep.* **3**, 2720; DOI:10.1038/srep02720 (2013).
2. Duan, X. F., Huang, Y., Agarwal, R. & Lieber, C. M. Single-nanowire electrically driven lasers. *Nature* **421**, 241–245 (2003).
3. Wang, J. Nanomaterial-based amplified transduction of biomolecular interactions. *Small* **1**, 1036–1043 (2005).
4. Zhao, Q. R., Xie, Y., Zhang, Z. G. & Bai, X. Size-selective synthesis of zinc sulfide hierarchical structures and their photocatalytic activity. *Cryst. Growth Des.* **7**, 153–158 (2007).
5. Zhou, X. L., Zhou, T. F., Hu, J. C. & Li, J. L. Controlled strategy to synthesize SnO_2 decorated SnS_2 nanosheets with enhanced visible light photocatalytic activity. *CrystEngComm* **14**, 5627–5633 (2012).
6. Wang, Z. W. *et al*. Morphology-tuned wurtzite-type ZnS nanobelts. *Nat. Mater.* **4**, 922–927 (2005).
7. Zhang, G. K., Shen, X. & Yang, Y. Q. Facile synthesis of monodisperse porous ZnO spheres by a soluble starch-assisted method and their photocatalytic activity. *J. Phys. Chem. C* **115**, 7145–7152 (2011).
8. Wei, X. W. *et al*. Large-scale controlled synthesis of FeCo nanocubes and microcages by wet chemistry. *Chem. Mater.* **20**, 6248–6253 (2008).
9. Chen, S. F., Tang, W. M., Hu, Y. F. & Fu, X. L. The preparation and characterization of composite bismuth tungsten oxide with enhanced visible light photocatalytic activity. *CrystEngComm* **15**, 7943–7950 (2013).
10. Sun, Y. Y., Wang, W. Z., Sun, S. M. & Zhang, L. A general synthesis strategy for one-dimensional Bi_2MO_6 (M = Mo, W) photocatalysts using an electrospinning method. *CrystEngComm* **15**, 7959–7964 (2013).
11. Yang, H. M., Li, M., Fu, L. J., Tang, A. D. & Mann, S. Controlled Assembly of Sb2S3 Nanoparticles on Silica/Polymer Nanotubes: Insights into the Nature of Hybrid Interfaces. *Sci. Rep.* **3**, 1336; DOI:10.1038/srep01336 (2013).
12. Zhang, Y., He, X., Ouyang, J. & Yang, H. M. Palladiumnanoparticles deposited on silanized halloysite nanotubes: synthesis, characterization and enhanced catalytic property. *Sci. Rep.* **3**, 2948; DOI:10.1038/srep02948 (2013).
13. Whitesides, G. & Grzybowski, B. Self-assembly at all scales. *Science* **295**, 2418–2421 (2002).
14. Ikkala, O. & Brinke, G. Hierarchical self-assembly in polymeric complexes: Towards functional materials. *Chem. Commun.* **19**, 2131–2137 (2004).
15. Chen, R. G., Bi, J. H., Wu, L., Li, Z. H. & Fu, X. Z. Orthorhombic Bi_2GeO_5 nanobelts: synthesis, characterization, and photocatalytic properties. *Cryst. Growth Des.* **9**, 1775–1779 (2009).
16. Chen, X. B., Shen, S. H., Guo, L. J. & Mao, S. S. Semiconductor-based photocatalytic hydrogen generation. *Chem. Rev.* **110**, 6503–6570 (2010).
17. Shang, M. *et al*. 3D Bi_2WO_6/TiO_2 hierarchical heterostructure: controllable synthesis and enhanced visible photocatalytic degradation performances. *J. Phys. Chem. C* **113**, 14727–14731 (2009).
18. Hou, D. F. *et al*. Electrospun sillenite $Bi_{12}MO_{20}$ (M = Ti, Ge, Si) nanofibers: general synthesis, band structure, and photocatalytic activity. *Phys. Chem. Chem. Phys.* **15**, 20698–20705 (2013).
19. Wei, W., Dai, Y. & Huang, B. B. First-principles characterization of Bi-based photocatalysts: $Bi_{12}TiO_{20}$, $Bi_2Ti_2O_7$, and $Bi_4Ti_3O_{12}$. *J. Phys. Chem. C* **113**, 5658–5663 (2009).
20. Cheng, H. F. *et al*. Tailoring AgI nanoparticles for the assembly of AgI/BiOI hierarchical hybrids with size-dependent photocatalytic activities. *J. Mater. Chem. A* **1**, 7131–7136 (2013).
21. He, C. H. & Gu, M. Y. Photocatalytic activity of bismuth germanate $Bi_{12}GeO_{20}$ powders. *Scripta Mater.* **54**, 1221–1225 (2006).
22. Abrahams, S. C., Jamieson, P. B. & Bernstein, J. L. Crystal structure of piezoelectric bismuth germanium oxide $Bi_{12}GeO_{20}$. *J. Chem. Phys.* **47**, 4034–4041 (1967).
23. Tapiero, M. & Launay, J. C. Photoconductivity study at room temperature of the undoped photorefractive $Bi_{12}GeO_{20}$. *Proc. SPIE Int. Soc. Opt. Eng.* **3801**, 271–278 (1999).
24. Li, X. X., Xiong, Y. J., Li, Z. Q. & Xie, Y. Large-scale fabrication of TiO_2 hierarchical hollow spheres. *Inorg. Chem.* **45**, 3493–3495 (2006).
25. Guo, Y. D., Zhang, G. K. & Gan, H. H. Synthesis, characterization and visible light photocatalytic properties of Bi_2WO_6/rectorite composites. *J. Colloid Interface Sci.* **369**, 323–329 (2012).
26. Wu, J., Duan, F., Zheng, Y. & Xie, Y. Synthesis of Bi_2WO_6 nanoplate-built hierarchical nest-like structures with visible-light-induced photocatalytic activity. *J. Phys. Chem. C* **111**, 12866–12871 (2007).
27. Liu, J., Zhang, G. K., Yu, J. C. & Guo, Y. D. In situ synthesis of Zn_2GeO_4 hollow spheres and their enhanced photocatalytic activity for the degradation of antibiotic metronidazole. *Dalton Trans.* **42**, 5092–5099 (2013).
28. Wang, Y. *et al*. Shape-controlled synthesis of palladium nanocrystals: A mechanistic understanding of the evolution from octahedrons to tetrahedrons. *Nano Lett.* **13**, 2276–2281 (2013).
29. Zheng, W., Wang, F. C. & Xu, Y. H. The growth and photorefractive effect of codoped Ce:Cu:BGO crystals. *Proc. SPIE Int. Soc. Opt. Eng.* **5636**, 651–659 (2005).
30. Marquet, H., Tapiero, M., Merle, J. C., Zielinger, J. P. & Launay, J. C. Determination of the factors controlling the optical background absorption in nominally undoped and doped sillenites. *Opt. Mater.* **11**, 53–65 (1998).
31. Wan, Z., Zhang, G. K., Wang, J. T. & Zhang, Y. L. Synthesis, characterization and visible-light photocatalytic activity of $Bi_{24}Al_2O_{39}$ mesoporous hollow spheres. *RSC Adv.* **3**, 19617–19623 (2013).
32. Li, S., Lin, Y. H., Zhang, B. P., Wang, Y. & Nan, C. W. Controlled fabrication of $BiFeO_3$ uniform microcrystals and their magnetic and photocatalytic behaviors. *J. Phys. Chem. C* **114**, 2903–2908 (2010).
33. Hou, D. F., Luo, W., Huang, Y. H., Yu, J. C. & Hu, X. L. Synthesis of porous $Bi_4Ti_3O_{12}$ nanofibers by electrospinning and their enhanced visible-light-driven photocatalytic properties. *Nanoscale* **5**, 2028–2035 (2013).
34. Aldrich, R. E., Hou, S. & Harvill, M. L. Electrical and Optical Properties of $Bi_{12}SiO_{20}$. *J. Appl. Phys.* **42**, 493 (1971).
35. Liu, H. & Wang, Z. L. Bismuth spheres grown in self-nested cavities in a silicon wafer. *J. Am. Chem. Soc.* **127**, 15322–15326 (2005).
36. Penn, R. L. & Banfield, J. F. Imperfect oriented attachment: dislocation generation in defect-free nanocrystals. *Science* **281**, 969–971 (1998).
37. Han, J. T. *et al*. Tunable synthesis of bismuth ferrites with various morphologies. *Adv. Mater.* **18**, 2145–2148 (2006).
38. Wang, X. & Li, Y. D. Synthesis and characterization of lanthanide hydroxide single-crystal nanowires. *Angew. Chem. Int. Ed.* **41**, 4790–4793 (2002).
39. Mills, A., Wang, J. S. & Ollis, D. F. Dependence of the kinetics of liquid-phase photocatalyzed reactions on oxygen concentration and light intensity. *J. Catal.* **243**, 1–6 (2006).
40. Sun, Q. & Xu, Y. M. Evaluating intrinsic photocatalytic activities of anatase and rutile TiO_2 for organic degradation in water. *J. Phys. Chem. C* **114**, 18911–18918 (2010).
41. Xu, Y. M. *et al*. Rate enhancement and rate inhibition of phenol degradation over irradiated anatase and rutile TiO_2 on the addition of NaF: New insight into the mechanism. *J. Phys. Chem. C* **111**, 19024–19032 (2007).
42. Chen, J. Y., Lim, B., Lee, E. P. & Xia, Y. N. Shape-controlled synthesis of platinum nanocrystals for catalytic and electrocatalytic applications. *Nano Today* **4**, 81–95 (2009).
43. Xia, X. H. & Xia, Y. N. Symmetry breaking during seeded growth of nanocrystals. *Nano Lett.* **12**, 6038–6042 (2012).
44. Xia, X. H. *et al*. On the role of surface diffusion in determining the shape or morphology of noble-metal nanocrystals. *Proc. Natl. Acad. Sci. U.S.A.* **17**, 6669–6673 (2013).

Acknowledgments

This work was supported by the National Basic Research Program of China (973 Program) 2013CB632402, SRFDP (20110143110015) and was partially supported by the NSFC (50872103).

Author contributions

G.K.Z. and Z.W. designed the research and wrote the manuscript. Z.W. performed the experiments and prepared all the figures. All authors reviewed the manuscript.

Additional information

Supplementary information accompanies this paper at http://www.nature.com/scientificreports

Competing financial interests: The authors declare no competing financial interests.

How to cite this article: Wan, Z. & Zhang, G. Controlled synthesis and visible light photocatalytic activity of $Bi_{12}GeO_{20}$ uniform microcrystals. *Sci. Rep.* **4**, 6298; DOI:10.1038/srep06298 (2014).

This work is licensed under a Creative Commons Attribution-NonCommercial-NoDerivs 4.0 International License. The images or other third party material in this article are included in the article's Creative Commons license, unless indicated otherwise in the credit line; if the material is not included under the Creative Commons license, users will need to obtain permission from the license holder in order to reproduce the material. To view a copy of this license, visit http://creativecommons.org/licenses/by-nc-nd/4.0/